Khosravi, V., Gholizadeh, A., Saberioon, M. (2022): Soil toxic elements determination using integration of Sentinel-2 and Landsat-8 images: Effect of fusion techniques on model performance. - Environmental Pollution, 310, 119828.

https://doi.org/10.1016/j.envpol.2022.119828

Journal Pre-proof

Soil toxic elements determination using integration of Sentinel-2 and Landsat-8 images: Effect of fusion techniques on model performance

Vahid Khosravi, Asa Gholizadeh, Mohammadmehdi Saberioon

PII: S0269-7491(22)01042-9

DOI: https://doi.org/10.1016/j.envpol.2022.119828

Reference: ENPO 119828

To appear in: *Environmental Pollution*

Received Date: 11 April 2022

Revised Date: 14 July 2022

Accepted Date: 19 July 2022

Please cite this article as: Khosravi, V., Gholizadeh, A., Saberioon, M., Soil toxic elements determination using integration of Sentinel-2 and Landsat-8 images: Effect of fusion techniques on model performance, *Environmental Pollution* (2022), doi: https://doi.org/10.1016/j.envpol.2022.119828.

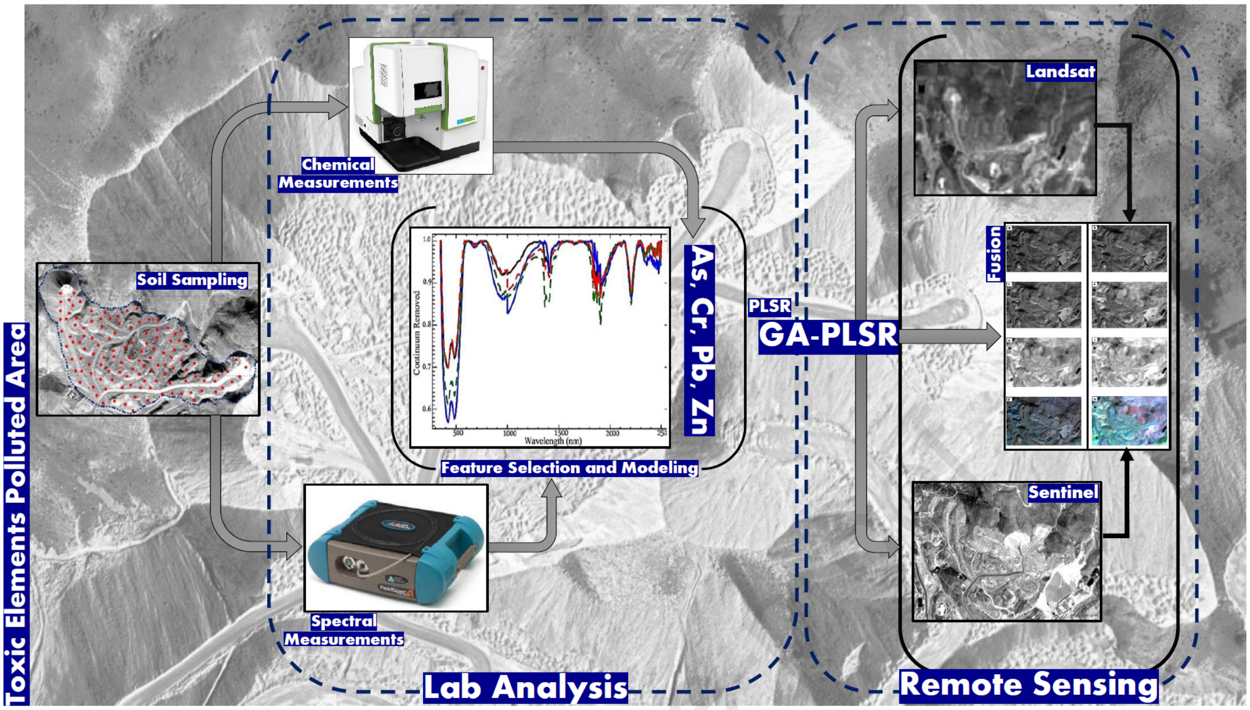
Toxic Elements Polluted Area
Soil Sampling
Chemical Measurements
Spectral Measurements
Feature Selection and Modeling
As, Cr, Pb, Zn
PLSR
GA-PLSR
Lab Analysis
Landsat
Fusion
Sentinel
Remote Sensing

Soil toxic elements determination using integration of Sentinel-2 and Landsat-8 images: Effect of fusion techniques on model performance

Vahid Khosravi[a], Asa Gholizadeh*[a], Mohammadmehdi Saberioon[b]

[a] *Department of Soil Science and Soil Protection, Faculty of Agrobiology, Food and Natural Resources, Czech University of Life Sciences Prague, Kamycka 129, Suchdol, Prague 16500, Czech Republic*
[b] *Helmholtz Centre Potsdam GFZ German Research Centre for Geosciences, Telegrafenberg, Potsdam 14473, Germany*

Abstract

Finding an appropriate satellite image as simultaneous as possible with the sampling time campaigns is challenging. Fusion can be considered as a method of integrating images and obtaining more pixels with higher spatial, spectral and temporal resolutions. This paper investigated the impact of Landsat 8-OLI and Sentinel-2A data fusion on prediction of several toxic elements at a mine waste dump. The 30 m spatial resolution Landsat 8-OLI bands were fused with the 10 m Sentinel-2A bands using various fusion techniques namely hue-saturation-value, Brovey, principal component analysis, Gram-Schmidt, wavelet, and area-to-point regression kriging (ATPRK). ATPRK was the best method preserving both spectral and spatial features of Landsat 8-OLI and Sentinel-2A after fusion. Furthermore, the partial least square regression (PLSR) model developed on genetic algorithm (GA)-selected laboratory visible-near infrared-shortwave infrared (VNIR–SWIR)

*Corresponding author, Email: gholizadeh@af.czu.cz

spectra yielded more accurate prediction results compared to the PLSR model calibrated on the entire spectra. It was hence, applied to both individual sensors and their ATPRK-fused image. In case of the individual sensors, except for As, Sentinel-2A provided more robust prediction models than Landsat 8-OLI. However, the best performances were obtained using the fused images, highlighting the potential of data fusion to enhance the toxic elements' prediction models.

Keywords: Soil contamination, data fusion, satellite image, Earth observation, genetic algorithm.

1. Introduction

The quality of soil directly affects the health of its organisms. However, soil is subjected to anthropogenic disturbance by various mining, industrial, and agricultural activities that leads to severe contamination. Among various soil contaminants, toxic elements are considered as significant threats to human and livestock health and food security (Xu et al., 2020; Järup, 2003; Jia et al., 2019). Therefore, monitoring the concentration and distribution of these types of contamination is a prerequisite for soil remediation projects. However, traditional sampling and laboratory analysis methods have always been costly and time-consuming (Kästner et al., 2022; Gholizadeh et al., 2021) and limited to sampled point locations and do not well specify the spatial distribution of contaminants. Hence, using a time- and cost-efficient technique with high spatial impact seems inevitable.

Application of visible–near infrared–shortwave infrared (VNIR–SWIR) reflectance spectroscopy has been investigated by some researchers for fast and non-destructive estimation and mapping of various toxic elements (Gholizadeh et al., 2018; Shi et al., 2018). The relationship between soil toxic elements and spectrally active attributes such as iron (Fe), soil organic carbon (SOC), and clay has also made it possible to monitor toxic elements on a large scale, using spectral data from airborne and spaceborne remote sensing (Heller Pearlshtien & Ben-Dor, 2020). For instance, Kemper & Sommer (2004) used airborne hyperspectral imagery provided by the HyMap sensor to map the distribution of lead (Pb) and chromium (Cr) in floodplains located in Spain. HyMap data was also used together with field spectroscopy to map toxic elements around a mining area in Spain (Choe et al., 2008). Recently, Hymap-C airborne hyperspectral imagery was successfully used in another study to estimate the distribution of soil toxic elements (i.e., As, Cr, Pb, and Zn) in Yitong County mining area in China (Tan et al., 2021). In addition, Simulated HyMap thematic mapper (TM) and QuickBird satellite images were used to predict the concentration of Ni, Cu, and Cr in soils of Baguazhou Island and Jiangning County in China (Wu et al., 2011). Moreover, Peng et al. (2016) used Landsat 8 multi-spectral images and successfully modeled and mapped the spatial distribution of arsenic (As), nickel (Ni), copper (Cu), zinc (Zn), Pb, and Cr in Qatari soils.

Most studies have used the images spectra and other ancillary data or environmental covariates to predict the distribution of toxic elements (Peng et al., 2016; Shi et al., 2018). Despite all efforts made, the successful estimation of the toxic elements by implementation of laboratory-based models on spectra of airborne and satellite imagery is limited to a few studies (Khosravi et al., 2021; Choe et al., 2008). One issue with this application is the gap between the soil sampling and image acquisition dates due to cloud or shadow in satellite images, which may cause differences in spectral characteristics of soil samples and co-located pixels in images. In this case, fusion can be used, as a solution, to increase the temporal resolution of images taken from a specific area.

In remote sensing, fusion is typically defined as integrating two or more images with different spectral and spatial features. In this way, the fusion product contains all features of both single images, hence, it is more informative (Palsson et al., 2018). The fusion process must preserve both spectral and spatial resolutions of the resulting fused image, while avoiding spectral and/or spatial distortion in it (Qu et al., 2018). Image fusion is performed at three different levels (Pohl & Van Genderen, 1998) namely, 1) decision level, 2) feature level, and 3) pixel level. At the decision (or interpretation) level, as the highest processing level, the input images are processed separately and the extracted information with different confidence degrees are then fused based on decision rules. In feature level, the input images' geometrical, structural, and spectral features are being derived and fused. Finally, in pixel level as the lowest processing level of image composition, input images are being fused using pixel-by-pixel values combination scenario (Ghassemian, 2016; Javan et al., 2021). The fusion algorithms at pixel level are generally divided into four classes of component substitution (CS), multiresolution analysis (MRA), Bayesian probability and variational Loncan et al. (2015); Yokoya et al. (2017). The CS approach, i.e., replacing one of the multispectral image components with the panchromatic (PAN) image, has been used more frequently along with the MRA in which the spatial details obtained by multiscale decomposition of the PAN image, are injected into the multispectral data Loncan et al. (2015). The state of the art geostatistical (e.g., area-to-point regression kriging (ATPRK)) and deep learning (e.g., convolutional neural networks (CNN) and enhanced super-resolution generative adversarial network (ESRGAN)) techniques have also gained popularity in recent years in fusion of multispectral images (Wang et al., 2017a; Lanaras et al., 2018; Salgueiro Romero et al., 2020; Gargiulo et al., 2019).

Sentinel-2 and Landsat 8 operational land imager (OLI) provide free medium-spatial resolution multispectral images for several fields of applications including soil contamination determination (Khosravi et al., 2021; Dkhala et al., 2020; Liu et al., 2018). Landsat 8-OLI and Sentinel-2 together provide an average revisit of 2.9 days (Li & Roy, 2017). Therefore, it is expected that their synergistic application will improve timely and accurate observations of the Earth's surface as well as their usage in different disciplines of remote sensing such as environmental research Agapiou (2020).

The current study aims to explore the potential of the individual images of Landsat 8-OLI and Sentinel-2A as well as their fusion on quantifying As, Pb, Zn, and Cr in Sarcheshmeh mine case study. For the fusion purpose, different techniques namely, hue-saturation-value (HSV), Brovey, principal component analysis (PCA), Gram-Schmidt (GS), wavelet, and ATPRK are tested. The main specific objective is to take full advantage of the information available in both Sentinel-2 and Landsat 8-OLI images to provide a quantitative outcome of the fusion process for assessing soil contamination. It is expected that the complementary effect of data fusion will have a promising influence on the toxic elements' prediction and mapping. The study also employs genetic algorithm (GA) to select important wavelengths of the lab spectra needed for developing the partial least square regression (PLSR) prediction models to assess the impact of variable selection on performance of the final models. Due to selection of wavelengths of greater importance using GA feature selection technique, the improvement of the toxic elements assessment is anticipated in lab spectroscopy and consequently, in satellite imaging.

2. Materials and methods

2.1. Study area, sample collection and analysis

This study was conducted in an inactive waste dump located at the north-eastern part of the main pit in Sarcheshmeh porphyry copper mine, southern Iran (Figure 1). Sarcheshmeh is Iran's largest mine and one of the world's largest porphyry copper mines in which sulphide rich waste rocks are accumulated and transported to certain areas known as waste dumps. Oxidation of sulphide minerals such as pyrite (FeS_2) in waste dumps produces large amounts of acid drainage that leaches toxic elements in the path through rocks and mining wastes, causing water and soil pollution in surrounding areas (Park et al., 2019; Rambabu et al., 2020; Simate, 2021).

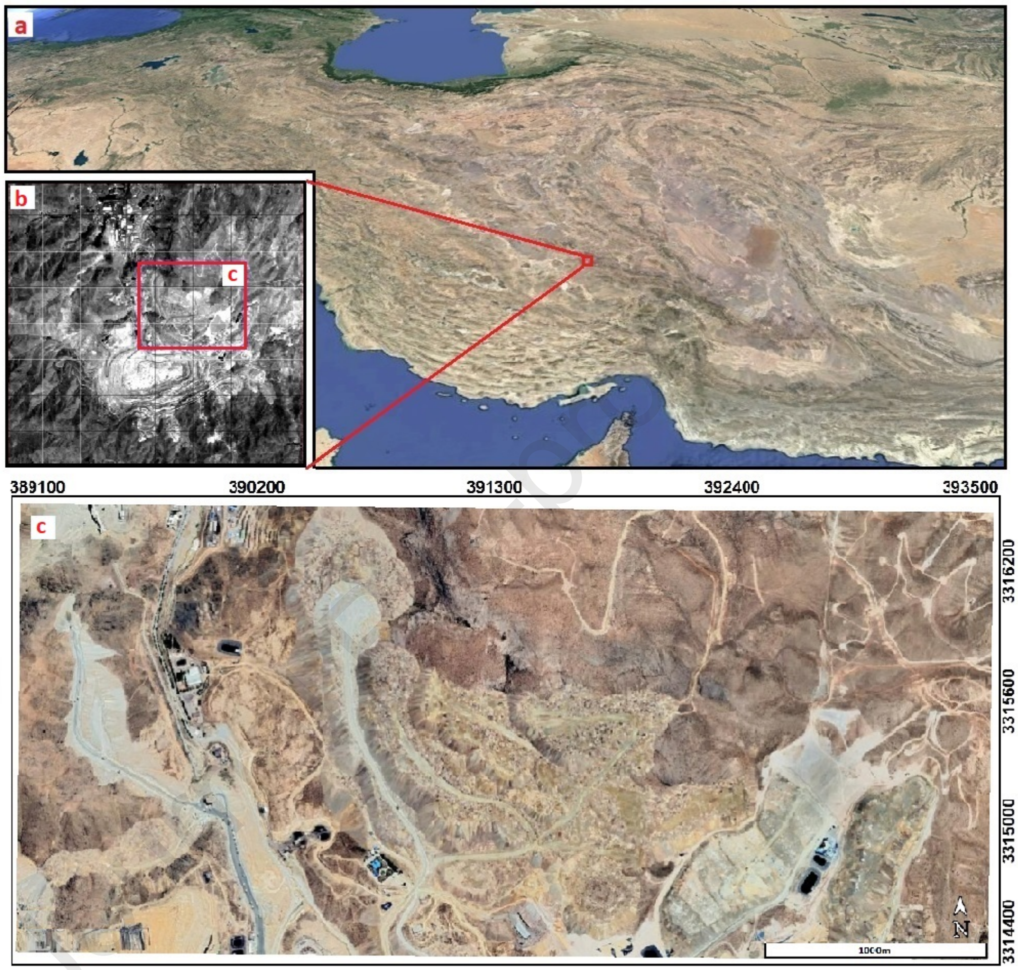

Area.jpg

Figure 1: Study area in Iran (a), in Sarcheshmeh copper complex (b), and in the waste dump (c).

One hundred and twenty (120) soil samples were collected on August 12th, 2015 from uniformly distributed predetermined points on the surface of the waste dump (depths 0 to 2 cm). The geographical locations of the sampling points were recorded using a global positioning system (GPS) instrument with an accuracy of ± 3 m. After being dried at 40° C, samples were pulverised to 200 mesh with the aim of minimizing the effect of particle size on soil reflectance spectra. They were then passed through a four mesh (4.76 mm) sieve, divided into two parts to be transferred to the laboratory for chemical and spectroscopic measurements. They were stored at ambient temperature until the chemical and spectral analyzes were performed.

Qualitative and quantitative analyses of clay minerals and Fe-oxides/hydroxides were performed through thin and polished sections and X-ray diffraction (XRD) at the Iran mineral processing center. The concentration of As, Pb, Zn, and Cr were measured using the inductively coupled plasma (ICP) analysis method (LabWest Minerals Analysis Pty Ltd., Malaga, WA, Australia).

2.2. Spectra measurement and pre-processing

In order to avoid spectral noise caused by water content of the soil, samples were dried at 105° C overnight (Lobell & Asner, 2002). Fieldspec 3 portable spectroradiometer (ASD Inc., Boulder, Co, USA) was employed to measure the samples' spectra in the laboratory. For each measurement, soil samples were placed into 2 cm diameter glass containers, forming a 10 cm layer of soil with a flat surface to guarantee maximum light reflection and a high signal-to-noise ratio (SNR). Three consecutive readings were recorded for every sample and their average was considered as the main spectra. After recording every ten samples, the spectrometer device was re-calibrated using a white $BaSO_4$ panel.

Afterwards, pre-processing was applied to the raw spectra. First, two very end parts (350 to 399 nm and 2451 to 2500 nm) were eliminated to remove noise at edges of the spectra. The reflectance spectra was then transformed into absorbance to avoid scattering effects (Kemper & Sommer, 2002).

Each sample's spectra was re-sampled into 10 nm wavelength intervals yielding 205 variables. In order to remove the artificial noise of the instrument, Savitzky-Golay (SG) smoothing (Savitzky & Golay, 1964) was implemented and followed by a polynomial first-derivative (FD) filter on the smoothed spectra. Outliers were also detected using PCA transformation as described in (Khosravi et al., 2021) and removed from further processing.

2.3. Satellite image selection and pre-processing

Freely available Landsat 8-OLI and Sentinel-2 satellites have bands, almost similar in terms of positions in both VNIR and SWIR regions (Table S1) and in terms of geometric accuracy (Earth Resources Observation and Science Center, 2019), which provide a great opportunity to fuse their data in order to provide more continuous monitoring at a large scale Wang et al. (2017a).

A standard L1T radiometric and geometric corrected Landsat 8-OLI image was downloaded from the United States geological survey (USGS) EarthExplorer website. Atmospheric correction was also performed using the fast line-of-sight atmospheric analysis of spectral hypercubes (FLAASH) algorithm (Cooley et al., 2002). The acquisition time of the image was on August 13th, 2015, very close to the soil sampling date. Moreover, a cloud-free level 1-C top of atmosphere (ToA) reflectance image of Sentinel-2 was acquired on January 20th, 2016, from the European space agency (ESA) open-access Copernicus hub. Atmospheric correction was performed through SNAP software with Sen2cor algorithm to convert ToA reflectance values to surface reflection.

2.4. Fusion approaches

Some of the most commonly used image fusion techniques including CS, HSV (Ehlers et al., 2010), Brovey (Ltd, 1990), GS (Laben & Brower, 2000), PCA Shah et al. (2008), and MRA-based wavelet Nunez et al. (1999) were used in this study, along with the novel geostatistics-based method of ATPRK proposed by Wang et al. (2015). In ATPRK, regression modeling and residual down-scaling are the two processing steps yielding $Z^l_{regression}(x)$ and $Z^l_{residual}(x)$, as the result of each step, respectively:

$$Z^l_F(x) = Z^l_{Regression}(x) + Z^l_{Residual}(x) \tag{1}$$

where $Z^l_F(x)$ is the ATPRK prediction. The general trend of the results for fine spatial resolution is achieved by the regression modeling, using Eq. 2:

$$Z^l_{Regression}(x_0) = \sum_{k=1}^{K} a_k Z^k_F(x_0) + b \tag{2}$$

where a_k is the fine band k weighting coefficient, and b is a constant. ATPK method is then used to down-scale the coarse residual image R^l_C obtained in the previous step:

$$Z^l_{Residual}(x_0) = \sum_{i=1}^{N} \lambda_i R^l_C(x_i), s.t. \sum_{i=1}^{N} \lambda_i = 1 \tag{3}$$

where $R^l_C(x_i)$ is the i_{th} neighbor relating residual. Kriging matrix is used to produce weights.

The two 20 m Sentinel-2A bands (bands 11 and 12) were firstly pan-sharpened to 10 m using all above mentioned fusion techniques, the best results were selected and then the 30 m pixel size bands 2–7 of Landsat 8-OLI were down-scaled to 10 m using the corresponding 10 m resolution Sentinel-2A bands (bands 2, 3, 4, 8, 11, and 12) (Table S1). All re-sampling in this study were performed using the nearest neighbor method. The resulting fused bands are shown with Greek letters of β, γ, δ, ϵ, ζ, η throughout the manuscript (Table S2).

2.5. Fusion evaluation criteria

A reference image is imperative for quantitative evaluation of the fusion product. As there was no such image available in our study, the coarse resolution bands were down-graded in spatial resolution (i.e., re-sampled to coarser resolution pixels) by a factor equal to the spatial resolution ratio of the original and fused images. The reference for evaluation of the fusion method would be the original image which is about to be fused Palsson et al. (2018). In our study, the Landsat 8-OLI 30 m pixel bands were down-graded by the factor of three to 90 m pixel size bands and the main 30 m pixel image was used as the reference for evaluation of the fusion techniques.

The performance of the fusion techniques was evaluated using three indicators, namely the spectral angle mapper (SAM), root mean square error (RMSE), and relative global dimensional synthesis error (ERGAS) Wald (2000). The overall spectral difference between the reference and fused images is calculated by RMSE. In SAM, the angle between two vectors is used to calculate their spectral similarity. The value of SAM for the whole image is the average of all angles obtained for every pixels of that image. ERGAS uses the mean square error (MSE) to calculate the degree of spectral/spatial distortion in the fused image (Eq. 4).

$$ERGAS = 100\frac{h}{l}\sqrt{\frac{1}{N}\sum_{k=1}^{N}(\frac{RMSE(k)}{Mean(k)})^2} \quad (4)$$

where, h/l is the ratio between spatial resolution of original and fused images, N denotes the number of the fused image bands, RMSE(k) indicates the root mean squared error of the k_{th} band between the fused and reference images, and finally Mean(k) is the mean value of differences between the k_{th} band of the reference and fused images. The optimal value for ERGAS and SAM is zero indicating no significant spectral difference between the original and fused images.

2.6. Determination of spectral similarity between samples and images spectra

The SAM (Kruse et al., 1993) method was applied to determine the degree of similarity between the laboratory reflectance spectra of each sample and the spectra of the same position pixel for all images used. This was conducted to investigate the possibility of applying prediction models on images spectra. The degree of spectral similarity was measured separately for the VNIR and SWIR spectral ranges.

In addition, statistical similarity between the spectral features of images and soil samples were tested using the one-way analysis of variance (ANOVA) method. In case of accepting the null hypothesis in ANOVA, there is no significant difference between the mean values of the laboratory reflectance spectra and the selected image features. The F-value was also calculated at the significant level of 0.05 to test the hypothesis. In case of any significant correlation, the spectral features of the image were used as independent variables in prediction of the models.

2.7. Model development

Before modeling to be conducted, a practical approach for improving the models' robustness is the elimination of irrelevant variables in the data and the selection of relevant spectral features and effective wavelengths (Xiaobo et al., 2010; Xu et al., 2020; Gholizadeh et al., 2021). In our study, GA was used to select the optimum input spectral variables of the models. GA is a particular class of evolutionary algorithms (EA), which uses mutation, natural selection, and crossover as techniques inspired by evolutionary biology (Goldberg & Holland, 1988; Katoch et al., 2020). In order to obtain an optimum selection, different values for GA parameters were tested and following parameters were obtained: population size = 100 chromosomes, cross-over ratio = 0.8, cross-over probability = 0.5, mutation rate = 0.01, mutation probability = 0.2, and number of iterations = 1000.

Partial least square regression (PLSR) and genetic algorithm-partial least square regression (GA-PLSR) techniques were applied on FD spectra to predict the concentrations of the toxic elements. The models were developed through the leave-one-out cross-validation (LOOCV) method on randomly selected 75% of the data (calibration/training dataset).

2.8. Model evaluation

Coefficient of determination (R^2), RMSE, and residual prediction deviation (RPD) were performed on the validation dataset to assess the performance of the models. R^2 and RMSE can be measured using the difference between the observed and predicted values. RPD is the ratio of standard deviation to RMSE. The reliability of the prediction models (quality and generalisation) can be defined based on five levels of RPD, including (Saeys et al., 2005; Magwaza et al., 2012): 1) unreliable (for values less than 1.5), 2) appropriate for rough predictions (between 1.5 and 2.0), 3) fit for quantitative predictions (between 2.0 and 2.5), 4) good models (between 2.5 and 3.0), and 5) satisfactory models (greater than 3.0).

Figure 2 illustrates the flowchart of the methodology used in this study.

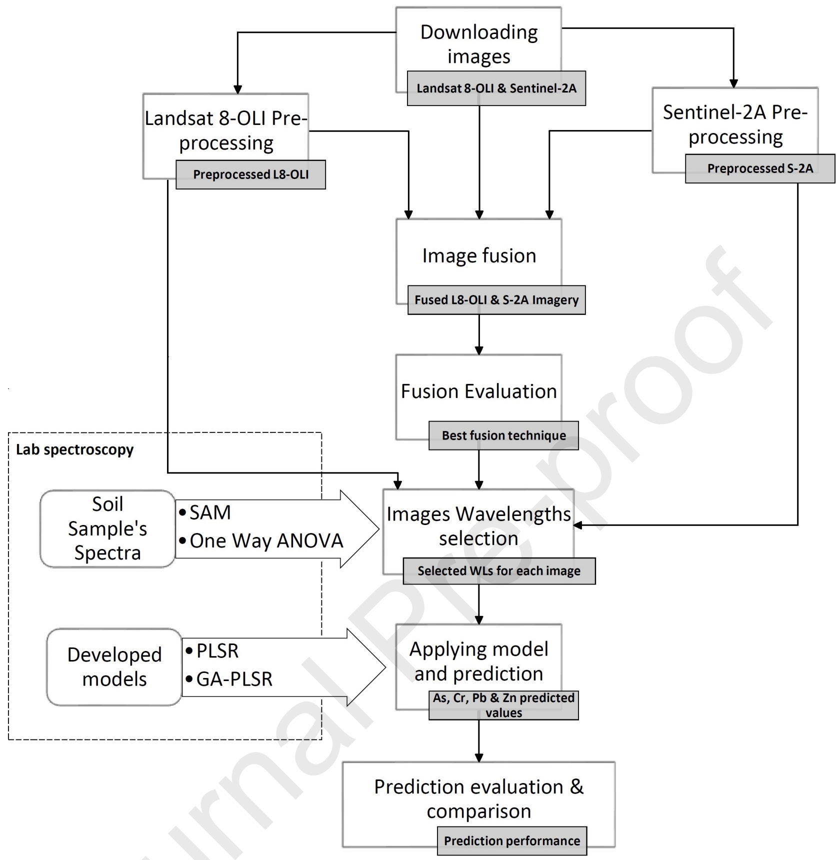

Figure 2: A concise description of procedures conducted in this study.

3. Results

3.1. Soil samples descriptive statistics and correlations

Table 1 shows descriptive statistics of the selected toxic elements concentrations along with their Fe-oxide/hydroxide and clay contents, as spectrally active soil properties.

Table 1: Descriptive statistics of the selected soil properties

Soil property	Min	Max	Mean	STD	Skewness	C.V. (%)
As ($mg.kg^{-1}$)	4.60	201	51.2	47.3	1.54	92
Cr ($mg.kg^{-1}$)	3.00	137	36.3	28.1	1.49	77
Pb ($mg.kg^{-1}$)	10.7	1562	251	308	2.39	122
Zn ($mg.kg^{-1}$)	60.0	3666	914	885	1.19	97
Fe (%)	1.16	25.3	12.3	6.14	-0.49	50
Clay (%)	6.04	8.44	7.46	0.56	-0.85	7.5
pH	2.08	7.53	4.76	1.31	0.25	28

Considering the permissible limits of As (20.0 $mg.kg^{-1}$ (Monchanin et al., 2021)), Cr (0.1 $mg.kg^{-1}$ (Kinuthia et al., 2020)), Pb (30.0 $mg.kg^{-1}$ (Monchanin et al., 2021)), and Zn (50 $mg.kg^{-1}$ (Denneman & Robberse, 1990)) in soils, the waste dump under study was considered as over-polluted. In addition, high values of STDs and CVs indicate the high heterogeneity of the dump, mainly due to accumulation from different areas of the mine. The pH values of the samples were between 2.08 to 7.53, with a mean value of 4.76, suggesting an acidic condition. Moreover, the Fe-oxides/hydroxides ranged between 1.16 and 25.3% , with a mean value of 12.3%. The average clay content was 7.46% with Min and Max values of 6.04% and 8.44%, respectively.

Figure S1 shows the histogram of toxic elements concentration in soil samples. Since the concentration values did not meet the requirements of a normal distribution, they were normalized using log-transformation (log10). Also, five samples were assumed as outliers, which were excluded from the dataset. All further analysis was thus performed on the remaining 115 samples.

In order to provide a general perspective on the relation of toxic elements concentrations with clay minerals and Fe-oxides/hydroxides (as soil spectrally active attributes), a correlation analysis was performed. As can be seen in Table S3, Cr had the highest absolute correlation value with clay minerals (r = 0.67) among the other toxic elements. However, the highest correlation of Fe-oxides/hydroxides was observed with As (r = 0.71). The highest correlation between all toxic elements was seen between Pb and Zn (r = 0.78).

3.2. Soil samples spectral information

The raw and continuum removed spectra of four randomly selected samples can be seen in our previous recent publication (Khosravi et al., 2021). Visual inspection of the spectra indicates that the overall reflectance trends and wave forms of the spectral curves of different samples were almost similar.

The relationship between soil's spectrally-active attributes and featureless toxic elements leads to determining their concentration. Table S4 highlights the correlation between the most important and frequently reported wavelengths of soil's spectrally-active attributes (Genú & Demattê, 2011; Kooistra et al., 2003; Madejova & Komadel, 2001; Clark et al., 1990; Khosravi et al., 2017; Chakraborty et al., 2017; Vicente & de Souza Filho, 2011) and the concentration of samples' toxic elements.

It can be seen that As had the highest correlation values with VNIR range wavelengths (Table S4). Visible (VIS) region contains the most important spectral range of Fe-oxides/hydroxides (Genú & Demattê, 2011), it thus highlights the higher importance of Fe-oxides/hydroxides for As prediction in comparison to clay minerals. Moreover, the key spectral wavelengths for predicting Cr concentration were at about 460, 560, 650, and 930 nm in VNIR range as well as at 1400, 1900, and 2200 nm in SWIR region. The higher correlation between Cr and SWIR wavelengths indicates the higher ability of clay minerals to absorb Cr rather than the Fe-oxides/hydroxides (Kooistra et al., 2003). Furthermore, according to the Table S4, the highest correlation for Pb was at about 1900 nm, while the highest correlation of Zn was at about 930 nm. High correlation coefficients peaks at about 1400 and 2200 nm indicate the internal link between clay minerals and Pb and Zn (Kooistra et al., 2003).

3.3. Toxic elements' prediction models

In this study, predicted models based on soil spectral data were obtained using PLSR approach on the entire FD spectra. In addition, models were developed using 31 spectral variables (wavelengths) selected through feature selection procedure conducted by GA method on the samples' laboratory FD spectra. The different models' evaluation statistics are shown in Table 2.

Table 2: Performance of toxic elements prediction models developed using the entire spectra (PLSR) and the selected wavelengths (GA-PLSR) (validation dataset)

Model	Toxic element	R_p^2	RPD	$RMSE_p$	Latent factor
PLSR	As	0.79	3.70	12.8	5
	Cr	0.53	1.82	15.4	5
	Pb	0.51	1.77	163	7
	Zn	0.48	1.64	494	8
GA-PLSR	As	0.88	5.02	9.42	4
	Cr	0.68	2.17	12.9	4
	Pb	0.63	2.07	135	4
	Zn	0.60	1.95	273	5

By comparing the predicted models' statistics, it can be concluded that the models developed on the GA-selected wavelengths had better performance than those constructed on the entire spectra. Accordingly, the best prediction model was developed for As using GA-PLSR with RPD = 5.02, $RMSE_p = 9.42$ mg.kg^{-1} , and $R^{2_p} = 0.88$, which is satisfactory according to the five levels quality criterion. This was followed by the model obtained for Cr (RPD = 2.17, $RMSE_p = 12.9$ mg.kg^{-1}, and $R^{2_p} = 0.68$). GA-PLSR models were also fit for quantitative prediction of Pb and appropriate for rough prediction of Zn. The poorest results were obtained by PLSR approach on Zn with RPD = 1.64, $RMSE_p = 494$ mg.kg^{-1}, and $R^{2_p} = 0.48$.

3.4. Performance of the fusion approaches

Comparing the performance of different methods on down-scaling the 20 m Sentinel-2A bands to 10 m, the best results were obtained using ATPRK followed by the GS method. However, the difference in evaluation criteria were not considerable between the two techniques. Therefore, due to complexity and high computation cost of ATPRK, we decided to use GS-produced 10 m images for further fusion steps. Figure 3 is the visual presentation of β bands obtained by fusion of bands 2 of Landsat 8-OLI and Sentinel-2A, using different fusion approaches. The first row presents the original individual images of Landsat 8-OLI and Sentinel-2A.

It can be seen that the spatial details within the dumpsite were clearly emerged in the fusion results indicating a dramatic spatial resolution improvement (Figure 3). Such details could not be recognized in the original 30 m pixel size Landsat 8-OLI individual image (Figure 3b). The access roads on the dumpsite and some facilities and constructions are observable in fused images obtained from all fusion techniques. However, the details visible in the resulting images were varied to some extent showing the different performance of the methods. Although the exact determination of the best fusion method requires quantitative assessments, scrutiny of the images reveals the superiority of GS, wavelet, and ATPRK through enhanced features in the dumpsite and nearby areas.

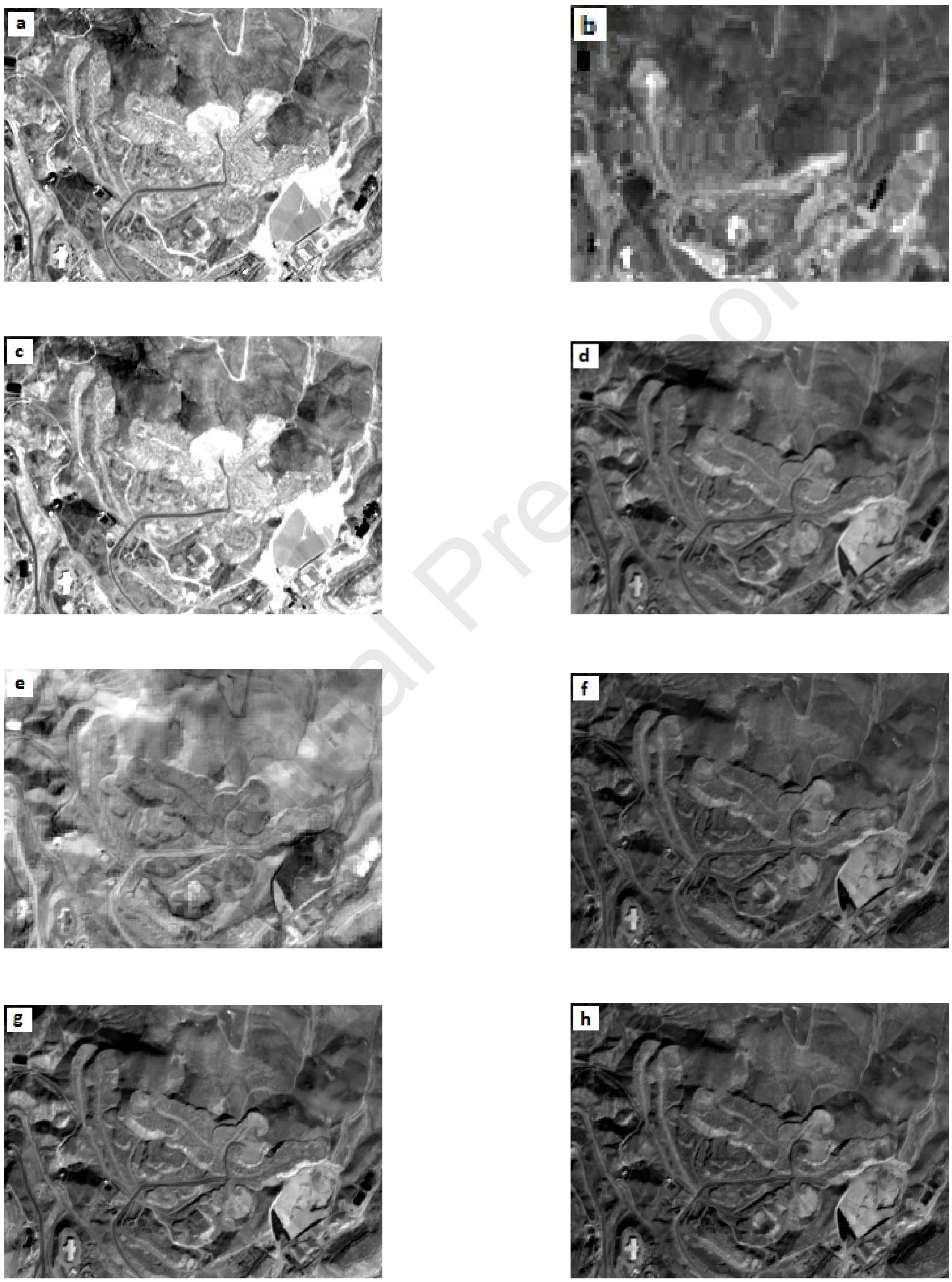

Figure 3: Visual comparison between original Sentinel-2A (a), original Landsat 8-OLI (b), β-band - HSV (c), β-band - Brovey (d), β-band - PCA (e), β-band - GS (f), β-band - wavelet (g), and β-band - ATPRK (h) images.

The quantitative performance of each fusion approach for integration of the Landsat 8-OLI and Sentinel-2A bands is shown in Table 3). As can be seen, the ATPRK considerably outperformed all other examined methods, providing lower values of each different criterion for all spectral bands. The wavelet and GS techniques yielded the second best results, while they had relatively the same performance by considering all bands and assessment metrics. Brovey, PCA, and HSV were in the next ranks.

Table 3: Quantitative assessment of the fusion approaches to integrate the Landsat 8-OLI and Sentinel-2A bands

Metric	Fusion approach	β	γ	δ	ϵ	ζ	η
RMSE	HSV	0.17	0.17	0.15	0.18	0.20	0.21
	Brovey	0.06	0.06	0.05	0.07	0.07	0.07
	GS	0.02	0.03	0.02	0.03	0.03	0.03
	PCA	0.12	0.13	0.10	0.13	0.14	0.15
	Wavelet	0.03	0.03	0.02	0.03	0.03	0.04
	ATPRK	0.01	0.01	0.01	0.01	0.01	0.02
SAM	HSV	3.17	3.28	3.11	3.34	3.35	3.56
	Brovey	2.10	2.18	2.03	2.31	2.34	2.37
	GS	0.97	1.13	0.96	1.14	1.17	1.29
	PCA	3.08	3.14	3.03	3.25	3.26	3.49
	Wavelet	0.98	1.08	0.93	1.19	1.24	1.26
	ATPRK	0.05	0.06	0.05	0.07	0.07	0.08
ERGAS	HSV	9.59	8.87	8.35	8.91	9.32	9.35
	Brovey	5.25	5.31	5.06	5.41	5.68	5.92
	GS	5.02	5.21	4.97	5.26	5.32	5.42
	PCA	8.14	8.25	7.06	8.35	8.41	8.56
	Wavelet	5.14	5.17	4.91	5.21	5.29	5.33
	ATPRK	2.93	2.99	2.78	3.11	3.16	3.26

As evidenced by the fusion results above, bands 4, which represent the red end of the VNIR spectra in both images, were fused to each other in the most efficient way. So that the lowest value of each evaluation criteria was obtained for the resulting band δ. As an example, for ATPRK, the values of 0.01, 0.05, and 2.78 were obtained for RMSE, SAM, and ERGAS, respectively. These values were lower comparing to those obtained for the other bands. Actually, the fusion performance was declined by the following order of bands β, γ, ϵ, ζ, and η (Table 3). This is in alignment with what can be visually observed in Figure S2.

3.5. Applying GA-PLSR model to the images

In order to evaluate the feasibility of applying GA-PLSR model on selected bands of the image pixels, the similarity between the samples' laboratory spectra and corresponding co-located pixels spectra were calculated. The obtained SAM values provided different degrees of similarity between different images and samples laboratory spectra (Table S5). SAM values between the lab spectra and Landsat 8-OLI, Sentinel-2A, and their ATPRK-based fusion were significantly lower (0.09, 0.09, and 0.06, respectively) in VNIR region compared to SWIR range (0.24, 0.19, and 0.16, respectively), which is mainly due to the better spectral resolution of all images in VNIR. Furthermore, the fused image of Landsat 8-OLI and Sentinel-2A showed more similarity to the spectral response of samples in both VNIR and SWIR regions.

Different static similarity thresholds have been proposed in the literature to recognize similar and dissimilar spectra (Shahriari et al., 2014). Considering the SAM values of lower than 0.3 as the threshold set for this study (Galal et al., 2012), GA-PLSR model could be applied to all three images spectral regions.

Table S6 shows the statistical difference (one-way ANOVA) between the mean reflectance values of the selected wavelengths of the samples' laboratory spectra and same location images pixels. According to the null hypothesis in one-way ANOVA, there was no significant difference between the mean values of the laboratory spectra and the image pixels spectra. This was tested by calculating the F-value at the significant level of 0.05.

It can be seen that in 460 nm, the P-values were higher than 0.05 for Sentinel-2A and the fused image. The corresponding F-values were less than the critical F indicating no significant difference is available between average spectral reflectance of the band in two datasets. In 530 nm, the statistical similarity was seen for Landsat 8-OLI and the fusion imagery. Spectral similarity was also found between laboratory spectra and corresponding pixels spectra of all three images in 650 nm (Table S6). Generally, similarity between laboratory and pixels spectra was observed for 6, 8, and 9 wavelengths for Landsat 8-OLI, Sentinel-2A, and their ATPRK-based fused image, respectively. The wavelengths with no significant difference and confirmed null hypothesis were used in the prediction models applied to the images.

The GA-PLSR models obtained for each toxic element were applied to wavelengths listed in Table S6 to predict the concentration of that specific element using spectra derived from the satellite imagery. Due to limited spectral ranges covering by the images, it was not possible to use all wavelengths formed the models. The comparison between the predicted and actual concentrations is given in the form of R^2, RMSE, and RPD assessment metrics in Table 4 .

Table 4: Performance of toxic elements prediction models developed by GA-PLSR applied to the images pixels spectra

Element	Metric	Sentinel-2A	Landsat 8-OLI	Sentinel-2A & Landsat 8-OLI (ATPRK)
As	R^2	0.52	0.58	0.69
	RMSE	32.43	21.78	18.23
	RPD	1.65	1.98	2.05
Cr	R^2	0.31	0.24	0.61
	RMSE	40.58	41.55	13.49
	RPD	1.12	1.05	1.78
Pb	R^2	0.29	0.21	0.58
	RMSE	312.89	349.85	129.57
	RPD	1.16	1.01	1.70
Zn	R^2	0.23	0.19	0.53
	RMSE	677.11	735.75	317.31
	RPD	1.09	1.02	1.62

Fusion of Landsat 8-OLI and Sentinel-2A yielded better prediction results for all toxic elements. The best prediction was obtained for As with R^2, RMSE, and RPD values of 0.69, 18.2 mg.kg^{-1}, and 2.05, respectively. This was followed by Cr, Pb, and Zn, which was compatible with the models prediction results obtained for the samples laboratory spectra (Table 2). Considering the individual Landsat 8-OLI and Sentinel-2A images, the performance of GA-PLSR model was better on Sentinel-2A data except for As, which Landsat 8-OLI provided better prediction results (Table 4).

In addition to down-scaling the synthetic Landsat 8-OLI 90 m pixel size data, the performance of various fusion methods was also evaluated in terms of predicting the concentration of toxic elements (Table S7). Obtaining results were in close agreement with those listed in Table 3. Applying GA-PLSR on ATPRK yielded the best prediction results followed by wavelet, GS, Brovey, PCA, and HSV, respectively. Therefore, this can be considered another criterion to prove the superiority of ATPRK over the other fusion methods.

4. Discussion

4.1. Feature selection and prediction models

The most important spectral range for Fe-oxides/hydroxides is the VIS range. Accordingly, the most significant spectral features were around 460, 500, 560, and 650 nm wavelengths (Khosravi et al., 2021), which occur mainly due to the electron transition of Fe^{3+} in Fe minerals such as goethite (FeOOH) and hematite (Fe_2O_3). The spectral range of 845–870 nm and 900–930 nm are also considered as hematite and goethite absorption areas (Genú & Demattê, 2011). In addition, the observed peaks in the NIR and SWIR regions are mainly associated with clay minerals (Kooistra et al., 2003). Furthermore, O-H bonds in hydroxyls or clay minerals such as muscovite, montmorionite, smectite, kaolinite, and illite cause obvious features in 1400 and 2200 nm (Madejova & Komadel, 2001). Also, the absorption peak in the 1900 nm is due to the O-H in water (Clark et al., 1990). Therefore, these important wavelengths and spectral regions along with those identified using GA feature selection method, were used for developing more robust prediction models.

The prediction models were then developed using PLSR and GA-PLSR techniques (Table 2) and it is apparent that GA-PLSR yielded better prediction performance than the general PLSR. This can be attributed to removing the uninformative wavelengths by GA and hence using the bands with greater importance, mentioned above, which resulted in the lowest $RMSE_p$. In a study by Gholizadeh et al. (2021), the superiority of GA was explained by its inherent ability in optimum selection of the spectral wavelengths. On the other hand, general PLSR faces a significant challenge dealing with the entire VNIR–SWIR spectra, which contains lots of redundant information (Wang et al., 2014). Various researchers obtained similar results, where GA-based selection of the spectral features has led to a better prediction performance of soil toxic elements (Wang et al., 2014; Sun et al., 2018; Zhang et al., 2019).

4.2. Fusion approaches

Valuable information is provided by the 10 m spatial resolution bands of Sentinel-2A. Therefore, in this study, we down-scaled the 30 m bands of Landsat 8-OLI (bands 2–7) to a finer spatial resolution of 10 m, with the aid of 10 m resolution data in the corresponding Sentinel-2A bands 2, 3, 4, 8, 11, and 12. Three types of image fusion approaches including component substitution, multi-resolution analysis, and geostatistical-based ATPRK were used to provide an acceptable comparison between different fusion techniques.

Visual and quantitative interpretations of the image fusion results (Figure 3 and Table 3) showed that the best fusion outcome was obtained by ATPRK method for each separate band. The superiority of ATPRK can be explained by the inherent ability of geostatistics in the analysis and prediction of spatial features. One other advantage of the ATPRK is that geostatistical methods can significantly preserve the spectral properties of the original Landsat coarse image (Wang et al., 2016c). The application of ATPRK fusion technique was initially used for down-scaling moderate resolution imaging spectroradiometer (MODIS) data (Wang et al., 2015). It was also successfully used in several fusion studies ever since (Wang et al., 2016c,a; Zhang et al., 2017; Wang et al., 2017b). Considering this, ATPRK has been used as a basis to develop geostatistics-based fusion techniques (Zhang et al., 2020; Dewage et al., 2020; Zhang et al., 2017; Wang et al., 2016b) or a benchmark to evaluate and compare the performance of other novel fusion methods (Shao et al., 2019; Nguyen et al., 2020, 2021).

By considering the fusion results using each of the sentinel-2A bands as the high spatial resolution panchromatic images (Table 3), those obtained using bands 11 and 12 (ζ and η, respectively), were not as satisfactory as what obtained using bands 2, 3, 4 and 8 (β, γ, δ and ϵ, respectively). This is because these bands originally were of 20 m pixel size, down-scaled to 10 m using the GS method. Therefore, this extra down-scaling process may cause the lower performance of the fusion methods yielded by using bands 11 and 12 of the Sentinel 2-A image. The 15 m spatial resolution panchromatic band of Landsat 8-OLI can also be used for the pan-sharpening, but the pixels of the resulting image are coarser than 10 m, which can be achieved by the Sentinel-2A data. The 5 m difference in spatial resolution is critical for monitoring toxic elements using the pixels spectra. One more problem is that, OLI bands 5–7 are not being covered by the wavelength of Landsat 8-OLI panchromatic band, which may cause lower fusion accuracy for these bands (Wang et al. (2017a).

Evaluating the performance of different fusion methods by synthetic data (down-scaling from 90 to 30 m in this study) may not be accurate enough. The main difference between down-scaling synthetic and original images is that finer spatial details must be restored in the original down-scaling (from 30 to 10 m in this study). It is therefore recommended that auxiliary data such as field samples, aerial photos, and high spatial resolution multispectral satellite imagery be used in future studies to evaluate the performance of fusion methods Wang et al. (2017a).

4.3. Models from individual and fused images spectra

Regardless of some gap in Landsat 8-OLI and Sentinel-2A images acquisition time, the best performance was generally obtained using the fused data. The time gap between the two images did not affect the fusion results' accuracy. This can mainly be explained by the inactivity of the waste dump, which led to minimum changes on the dump surface. Actually, no waste materials were dumped there during the time between the two images acquisition and even after that. Moreover, no vegetation can germinate and grow in that waste dump mostly due to acidic condition and loss of organic carbon and required nutrients. Furthermore, Sarcheshmeh is located in a semi-arid area with low precipitation rate (Khosravi et al., 2017), particularly during summer and autumn (the time between two images). The results of this study were comparable to the best of those obtained by (Wang et al., 2017a), in which the fusion performance of ATPRK and some other methods were compared under different time intervals between Landsat 8-OLI and Sentinel-2A images. Although fusion of images with shorter time gaps performed better in that study, all others were still fairly acceptable.

In terms of the prediction results obtained for each toxic element using PLSR on the GA-selected wavelengths (Table 4), the higher performance of the fusion product compared to the Landsat 8-OLI is linked to its better spatial resolution. The main reason for superiority of the fused imagery performance compared to Sentinel-2A can be attributed to the lower time gap between the sampling time and Landsat 8-OLI image acquisition time, which leads to lower spectral and radiometric differences between the fused imagery and samples' spectra. However, better prediction results of fused imagery for As and Cr can also be linked to better spectral coverage in VNIR region in which Fe-oxides/hydroxides have strong spectral features. The same reason justifies better As prediction results of individual Landsat 8-OLI image compared to the Sentinel-2A. For the other toxic elements, higher spatial and spectral resolution of Sentinel-2A over Landsat 8-OLI led to development of more robust prediction models from individual Sentinel-2A spectral bands in spite of the 5 months gap between field sampling and image acquisition time.

Despite the promising results obtained by ATPRK fusion approach, there are some issues associated with this kind of geostatistics-based methods. They entail complicated semi-variogram modeling based on the co-kriging matrix, which is computationally impractical for a broad domain. Furthermore, ATPRK may not be appropriate for locations where land cover is rapidly changing. As an alternative, other novel fusion techniques such as deep learning-based methods can be investigated in future studies to improve toxic elements prediction results. It is expected that the proposed methodology and developed models can be applied in other locations with similar terrestrial and particularly soil and climate conditions without any need to new soil sample collection; however, for applying the developed models in another location with different soil and climate conditions, new soil sampling is suggested. Nevertheless, it's anticipated that in near future, progress in developing new technologies and algorithms in satellite sensors and processing algorithms will pave the way for conducting these techniques with minimum requirement to ground-based measurements. As a future study, transferability of the obtained GA-PLSR models for predicting soil toxic elements in different geographical locations can be investigated. In addition, The sensitivity of the proposed methodology on various levels of toxic elements as well as its capability on detection of other soil contaminants such as acid drainage and petroleum hydrocarbons can further be explored.

Conclusions

According to the results of this study, compared to pixels' spectra of individual Sentinel-2A and Landsat 8-OLI imagery, the pixels' spectra of their fusion product showed the highest similarity to the spectral response of the samples measured in the laboratory, particularly in the VNIR region. One-way ANOVA method also yielded more similar wavelengths between the laboratory and fused image pixels spectra. Considering the individual Landsat 8-OLI and Sentinel-2A images, the performance of GA-PLSR model was better on Sentinel-2A data except for As that Landsat8-OLI provided better prediction results. Applying the GA-PLSR model on the ATPRK-fused image could produce more accurate predictions, for all the examined toxic elements, than the other fusion techniques. In all, this study concluded the fusion of Landsat 8-OLI and Sentinel-2A images could enhance the performance of soil toxic elements prediction models.

Agapiou, A. (2020). Evaluation of landsat 8 oli/tirs level-2 and sentinel 2 level-1c fusion techniques intended for image segmentation of archaeological landscapes and proxies. *Remote Sensing*, *12*, 579.

Chakraborty, S., Weindorf, D. C., Deb, S., Li, B., Paul, S., Choudhury, A., & Ray, D. P. (2017). Rapid assessment of regional soil arsenic pollution risk via diffuse reflectance spectroscopy. *Geoderma*, *289*, 72–81.

Choe, E., van der Meer, F., van Ruitenbeek, F., van der Werff, H., de Smeth, B., & Kim, K.-W. (2008). Mapping of heavy metal pollution in stream sediments using combined geochemistry, field spectroscopy, and hyperspectral remote sensing: A case study of the rodalquilar mining area, se spain. *Remote Sensing of Environment*, *112*, 3222–3233.

Clark, R. N., King, T. V., Klejwa, M., Swayze, G. A., & Vergo, N. (1990). High spectral resolution reflectance spectroscopy of minerals. *Journal of Geophysical Research: Solid Earth*, *95*, 12653–12680.

Cooley, T., Anderson, G. P., Felde, G. W., Hoke, M. L., Ratkowski, A. J., Chetwynd, J. H., Gardner, J. A., Adler-Golden, S. M., Matthew, M. W., Berk, A. et al. (2002). Flaash, a modtran4-based atmospheric correction algorithm, its application and validation. In *IEEE International Geoscience and Remote Sensing Symposium* (pp. 1414–1418). IEEE volume 3.

Denneman, C. A., & Robberse, J. G. (1990). Ecotoxicological risk assessment as a base for development of soil quality criteria. In *Contaminated Soil'90* (pp. 157–164). Springer.

Dewage, S. N. S. P., Minasny, B., & Malone, B. (2020). Disaggregating a regional-extent digital soil map using bayesian area-to-point regression kriging for farm-scale soil carbon assessment. *Soil*, *6*, 359–369.

Dkhala, B., Mezned, N., Gomez, C., & Abdeljaouad, S. (2020). Hyperspectral field spectroscopy and sentinel-2 multispectral data for minerals with high pollution potential content estimation and mapping. *Science of The Total Environment*, *740*, 140160.

Earth Resources Observation and Science Center (2019). Comparison of Sentinel-2 and Landsat. URL: `https://www.usgs.gov/centers/eros/science/usgs-eros-archive-sentinel-2-comparison-sentinel-2-and-landsat#overview` accessed:2022-02-09.

Ehlers, M., Klonus, S., Johan Åstrand, P., & Rosso, P. (2010). Multi-sensor image fusion for pansharpening in remote sensing. *International Journal of Image and Data Fusion*, *1*, 25–45.

Galal, A., Hassan, H., & Imam, I. F. (2012). A novel approach for measuring hyperspectral similarity. *Applied Soft Computing*, *12*, 3115–3123.

Gargiulo, M., Mazza, A., Gaetano, R., Ruello, G., & Scarpa, G. (2019). Fast super-resolution of 20 m sentinel-2 bands using convolutional neural networks. *Remote Sensing*, *11*, 2635.

Genú, A. M., & Demattê, J. A. M. (2011). Prediction of soil chemical attributes using optical remote sensing. *Acta Scientiarum. Agronomy*, *33*, 723–727.

Ghassemian, H. (2016). A review of remote sensing image fusion methods. *Information Fusion*, *32*, 75–89.

Gholizadeh, A., Coblinski, J. A., Saberioon, M., Ben-Dor, E., Drábek, O., Demattê, J. A., Borvka, L., Němeček, K., Chabrillat, S., & Dajčl, J. (2021). vis–nir and xrf data fusion and feature selection to estimate potentially toxic elements in soil. *Sensors*, *21*, 2386.

Gholizadeh, A., Saberioon, M., Ben-Dor, E., & Borvka, L. (2018). Monitoring of selected soil contaminants using proximal and remote sensing techniques: Background, state-of-the-art and future perspectives. *Critical Reviews in Environmental Science and Technology*, *48*, 243–278.

Goldberg, D. E., & Holland, J. H. (1988). Genetic algorithms and machine learning, .

Heller Pearlshtien, D., & Ben-Dor, E. (2020). Effect of organic matter content on the spectral signature of iron oxides across the vis–nir spectral region in artificial mixtures: An example from a red soil from israel. *Remote Sensing*, *12*. doi:10.3390/rs12121960.

Järup, L. (2003). Hazards of heavy metal contamination. *British medical bulletin*, *68*, 167–182.

Javan, F. D., Samadzadegan, F., Mehravar, S., Toosi, A., Khatami, R., & Stein, A. (2021). A review of image fusion techniques for pan-sharpening of high-resolution satellite imagery. *ISPRS Journal of Photogrammetry and Remote Sensing*, *171*, 101–117.

Jia, X., Hu, B., Marchant, B. P., Zhou, L., Shi, Z., & Zhu, Y. (2019). A methodological framework for identifying potential sources of soil heavy metal pollution based on machine learning: A case study in the yangtze delta, china. *Environmental Pollution*, *250*, 601–609.

Kästner, F., Sut-Lohmann, M., Ramezany, S., Raab, T., Feilhauer, H., & Chabrillat, S. (2022). Estimating heavy metal concentrations in technosols with reflectance spectroscopy. *Geoderma*, *406*, 115512.

Katoch, S., Chauhan, S. S., & Kumar, V. (2020). A review on genetic algorithm: past, present, and future. *Multimedia Tools and Applications*, (pp. 1–36).

Kemper, T., & Sommer, S. (2002). Estimate of heavy metal contamination in soils after a mining accident using reflectance spectroscopy. *Environmental science & technology*, *36*, 2742–2747.

Kemper, T., & Sommer, S. (2004). Use of airborne hyperspectral data to estimate residual heavy metal contamination and acidification potential in the guadiamar floodplain andalusia, spain after the aznacollar mining accident. In *Remote Sensing for Environmental Monitoring, GIS Applications, and Geology IV* (pp. 224–234). International Society for Optics and Photonics volume 5574.

Khosravi, V., Ardejani, F. D., Gholizadeh, A., & Saberioon, M. (2021). Satellite imagery for monitoring and mapping soil chromium pollution in a mine waste dump. *Remote Sensing*, *13*, 1277.

Khosravi, V., Ardejani, F. D., & Yousefi, S. (2017). Spectroscopic-based assessment of the content and geochemical behaviour of arsenic in a highly heterogeneous sulphide-rich mine waste dump. *Environmental Earth Sciences*, *76*, 1–16.

Kinuthia, G. K., Ngure, V., Beti, D., Lugalia, R., Wangila, A., & Kamau, L. (2020). Levels of heavy metals in wastewater and soil samples from open drainage channels in nairobi, kenya: Community health implication. *Scientific reports*, *10*, 1–13.

Kooistra, L., Wanders, J., Epema, G., Leuven, R., Wehrens, R., & Buydens, L. (2003). The potential of field spectroscopy for the assessment of sediment properties in river floodplains. *Analytica Chimica Acta*, *484*, 189–200.

Kruse, F. A., Lefkoff, A., Boardman, J., Heidebrecht, K., Shapiro, A., Barloon, P., & Goetz, A. (1993). The spectral image processing system (sips)—interactive visualization and analysis of imaging spectrometer data. *Remote sensing of environment*, *44*, 145–163.

Laben, C. A., & Brower, B. V. (2000). Process for enhancing the spatial resolution of multispectral imagery using pan-sharpening. US Patent 6,011,875.

Lanaras, C., Bioucas-Dias, J., Galliani, S., Baltsavias, E., & Schindler, K. (2018). Super-resolution of sentinel-2 images: Learning a globally applicable deep neural network. *ISPRS Journal of Photogrammetry and Remote Sensing*, *146*, 305–319.

Li, J., & Roy, D. P. (2017). A global analysis of sentinel-2a, sentinel-2b and landsat-8 data revisit intervals and implications for terrestrial monitoring. *Remote Sensing*, *9*, 902.

Liu, M., Wang, T., Skidmore, A. K., & Liu, X. (2018). Heavy metal-induced stress in rice crops detected using multi-temporal sentinel-2 satellite images. *Science of the total environment*, *637*, 18–29.

Lobell, D. B., & Asner, G. P. (2002). Moisture effects on soil reflectance. *Soil Science Society of America Journal*, *66*, 722–727.

Loncan, L., De Almeida, L. B., Bioucas-Dias, J. M., Briottet, X., Chanussot, J., Dobigeon, N., Fabre, S., Liao, W., Licciardi, G. A., Simoes, M. et al. (2015). Hyperspectral pansharpening: A review. *IEEE Geoscience and remote sensing magazine*, *3*, 27–46.

Ltd, E. R. M. P. (1990). The brovey transform explained. In *EMU Forum*. volume 2.

Madejova, J., & Komadel, P. (2001). Baseline studies of the clay minerals society source clays: infrared methods. *Clays and clay minerals*, *49*, 410–432.

Magwaza, L. S., Opara, U. L., Terry, L. A., Landahl, S., Cronje, P. J., Nieuwoudt, H., Mouazen, A. M., Saeys, W., & Nicolaï, B. M. (2012). Prediction of 'nules clementine'mandarin susceptibility to rind breakdown disorder using vis/nir spectroscopy. *Postharvest Biology and Technology*, *74*, 1–10.

Monchanin, C., Devaud, J.-M., Barron, A. B., & Lihoreau, M. (2021). Current permissible levels of metal pollutants harm terrestrial invertebrates. *Science of the Total Environment*, *779*, 146398.

Nguyen, H. V., Ulfarsson, M. O., & Sveinsson, J. R. (2021). Sharpening the 20 m bands of sentinel-2 image using an unsupervised convolutional neural network. In *2021 IEEE International Geoscience and Remote Sensing Symposium IGARSS* (pp. 2875–2878). IEEE.

Nguyen, H. V., Ulfarsson, M. O., Sveinsson, J. R., & Sigurdsson, J. (2020). Zero-shot sentinel-2 sharpening using a symmetric skipped connection convolutional neural network. In *IGARSS 2020-2020 IEEE International Geoscience and Remote Sensing Symposium* (pp. 613–616). IEEE.

Nunez, J., Otazu, X., Fors, O., Prades, A., Pala, V., & Arbiol, R. (1999). Multiresolution-based image fusion with additive wavelet decomposition. *IEEE Transactions on Geoscience and Remote sensing*, *37*, 1204–1211.

Palsson, F., Sveinsson, J. R., & Ulfarsson, M. O. (2018). Sentinel-2 image fusion using a deep residual network. *Remote Sensing*, *10*, 1290.

Park, I., Tabelin, C. B., Jeon, S., Li, X., Seno, K., Ito, M., & Hiroyoshi, N. (2019). A review of recent strategies for acid mine drainage prevention and mine tailings recycling. *Chemosphere*, *219*, 588–606.

Peng, Y., Kheir, R. B., Adhikari, K., Malinowski, R., Greve, M. B., Knadel, M., & Greve, M. H. (2016). Digital mapping of toxic metals in qatari soils using remote sensing and ancillary data. *Remote Sensing*, *8*, 1003.

Pohl, C., & Van Genderen, J. L. (1998). Review article multisensor image fusion in remote sensing: concepts, methods and applications. *International journal of remote sensing*, *19*, 823–854.

Qu, J., Lei, J., Li, Y., Dong, W., Zeng, Z., & Chen, D. (2018). Structure tensor-based algorithm for hyperspectral and panchromatic images fusion. *Remote Sensing*, *10*, 373.

Rambabu, K., Banat, F., Pham, Q. M., Ho, S.-H., Ren, N.-Q., & Show, P. L. (2020). Biological remediation of acid mine drainage: Review of past trends and current outlook. *Environmental Science and Ecotechnology*, *2*, 100024.

Saeys, W., Mouazen, A. M., & Ramon, H. (2005). Potential for onsite and online analysis of pig manure using visible and near infrared reflectance spectroscopy. *Biosystems engineering*, *91*, 393–402.

Salgueiro Romero, L., Marcello, J., & Vilaplana, V. (2020). Super-resolution of sentinel-2 imagery using generative adversarial networks. *Remote Sensing*, *12*, 2424.

Savitzky, A., & Golay, M. J. (1964). Smoothing and differentiation of data by simplified least squares procedures. *Analytical chemistry*, *36*, 1627–1639.

Shah, V. P., Younan, N. H., & King, R. L. (2008). An efficient pan-sharpening method via a combined adaptive pca approach and contourlets. *IEEE transactions on geoscience and remote sensing*, *46*, 1323–1335.

Shahriari, H., Ranjbar, H., Honarmand, M., & Carranza, E. J. M. (2014). Selection of less biased threshold angles for sam classification using the real value–area fractal technique. *Resource Geology*, *64*, 301–315.

Shao, Z., Cai, J., Fu, P., Hu, L., & Liu, T. (2019). Deep learning-based fusion of landsat-8 and sentinel-2 images for a harmonized surface reflectance product. *Remote Sensing of Environment*, *235*, 111425.

Shi, T., Guo, L., Chen, Y., Wang, W., Shi, Z., Li, Q., & Wu, G. (2018). Proximal and remote sensing techniques for mapping of soil contamination with heavy metals. *Applied Spectroscopy Reviews*, *53*, 783–805.

Simate, G. S. (2021). Environmental and health effects of acid mine drainage. In *Acid Mine Drainage* (pp. 97–114). CRC Press.

Sun, W., Zhang, X., Sun, X., Sun, Y., & Cen, Y. (2018). Predicting nickel concentration in soil using reflectance spectroscopy associated with organic matter and clay minerals. *Geoderma*, *327*, 25–35.

Tan, K., Ma, W., Chen, L., Wang, H., Du, Q., Du, P., Yan, B., Liu, R., & Li, H. (2021). Estimating the distribution trend of soil heavy metals in mining area from hymap airborne hyperspectral imagery based on ensemble learning. *Journal of Hazardous Materials*, *401*, 123288.

Vicente, L. E., & de Souza Filho, C. R. (2011). Identification of mineral components in tropical soils using reflectance spectroscopy and advanced spaceborne thermal emission and reflection radiometer (aster) data. *Remote Sensing of Environment*, *115*, 1824–1836.

Wald, L. (2000). Quality of high resolution synthesised images: Is there a simple criterion? In *Third conference" Fusion of Earth data: merging point measurements, raster maps and remotely sensed images"* (pp. 99–103). SEE/URISCA.

Wang, J., Cui, L., Gao, W., Shi, T., Chen, Y., & Gao, Y. (2014). Prediction of low heavy metal concentrations in agricultural soils using visible and near-infrared reflectance spectroscopy. *Geoderma*, *216*, 1–9.

Wang, Q., Blackburn, G. A., Onojeghuo, A. O., Dash, J., Zhou, L., Zhang, Y., & Atkinson, P. M. (2017a). Fusion of landsat 8 oli and sentinel-2 msi data. *IEEE Transactions on Geoscience and Remote Sensing*, *55*, 3885–3899.

Wang, Q., Rodriguez-Galiano, V., & Atkinson, P. M. (2017b). Geostatistical solutions for downscaling remotely sensed land surface temperature. *International Archives of the Photogrammetry, Remote Sensing and Spatial Information Sciences*, *42*.

Wang, Q., Shi, W., & Atkinson, P. M. (2016a). Area-to-point regression kriging for pan-sharpening. *ISPRS journal of photogrammetry and remote sensing*, *114*, 151–165.

Wang, Q., Shi, W., Atkinson, P. M., & Wei, Q. (2016b). Approximate area-to-point regression kriging for fast hyperspectral image sharpening. *IEEE Journal of Selected Topics in Applied Earth Observations and Remote Sensing*, *10*, 286–295.

Wang, Q., Shi, W., Atkinson, P. M., & Zhao, Y. (2015). Downscaling modis images with area-to-point regression kriging. *Remote Sensing of Environment*, *166*, 191–204.

Wang, Q., Shi, W., Li, Z., & Atkinson, P. M. (2016c). Fusion of sentinel-2 images. *Remote sensing of environment*, *187*, 241–252.

Wu, Y., Zhang, X., Liao, Q., & Ji, J. (2011). Can contaminant elements in soils be assessed by remote sensing technology: A case study with simulated data. *Soil science*, *176*, 196–205.

Xiaobo, Z., Jiewen, Z., Povey, M. J., Holmes, M., & Hanpin, M. (2010). Variables selection methods in near-infrared spectroscopy. *Analytica chimica acta*, *667*, 14–32.

Xu, D., Chen, S., Xu, H., Wang, N., Zhou, Y., & Shi, Z. (2020). Data fusion for the measurement of potentially toxic elements in soil using portable spectrometers. *Environmental Pollution*, *263*, 114649.

Yokoya, N., Grohnfeldt, C., & Chanussot, J. (2017). Hyperspectral and multispectral data fusion: A comparative review of the recent literature. *IEEE Geoscience and Remote Sensing Magazine*, *5*, 29–56.

Zhang, X., Sun, W., Cen, Y., Zhang, L., & Wang, N. (2019). Predicting cadmium concentration in soils using laboratory and field reflectance spectroscopy. *Science of the Total Environment*, *650*, 321–334.

Zhang, Y., Atkinson, P. M., Ling, F., Foody, G. M., Wang, Q., Ge, Y., Li, X., & Du, Y. (2020). Object-based area-to-point regression kriging for pansharpening. *IEEE Transactions on Geoscience and Remote Sensing*, .

Zhang, Y., Atkinson, P. M., Ling, F., Wang, Q., Li, X., Shi, L., & Du, Y. (2017). Spectral–spatial adaptive area-to-point regression kriging for modis image downscaling. *IEEE Journal of Selected Topics in Applied Earth Observations and Remote Sensing*, *10*, 1883–1896.

Declaration of interests

☒ The authors declare that they have no known competing financial interests or personal relationships that could have appeared to influence the work reported in this paper.

☐ The authors declare the following financial interests/personal relationships which may be considered as potential competing interests: